Eur. Phys. J. B **79**, 35–46 (2011)
DOI: 10.1140/epjb/e2010-10572-3

THE EUROPEAN PHYSICAL JOURNAL B

Regular Article

Structure and stability of annular sheared channel flows: effects of confinement, curvature and inertial forces – waves

E. Plaut[1,a], Y. Lebranchu[1,2], M. Jenny[1], and É. Serre[3]

[1] LEMTA, Nancy-Université & CNRS, 2 avenue de la Forêt de Haye, 54516 Vandœuvre Cedex, France
[2] AREVA NP, 1 place Jean Millier, 92084 Paris La Défense, France
[3] M2P2, CNRS & Aix-Marseille-Université, 38 rue Frédéric Joliot-Curie, 13451 Marseille Cedex 20, France

Received 23 July 2010 / Received in final form 29 November 2010
Published online 6 January 2011 – © EDP Sciences, Società Italiana di Fisica, Springer-Verlag 2011

Abstract. The structure and stability of the flows in an annular channel sheared by a rotating lid are investigated experimentally, theoretically and numerically. The channel has a square section, and a small curvature parameter: the ratio Γ of the inter-radii to the mean radius is 9.5%. The sidewalls and the bottom of the channel are integral and can rotate independently of the lid, permitting pure shear, co-rotation and counter-rotation cases. The basic flows obtained at small shear are characterized. In the absence of co-rotation, the centrifugal force linked with the curvature of the system plays an important role, whereas, when co-rotation is fast, the Coriolis force dominates. These basic flows undergo some instabilities when the shear is increased. These instabilities lead to supercritical traveling waves in the pure shear and co-rotation cases, but to weak turbulence in the counter-rotation case. The Reynolds number for the onset of instabilities, constructed with the velocity difference between the lid and bottom at mid-radius, and the height of the channel, increases from 1000 in the counter-rotation case to 1260 in the pure shear case and higher and higher values when co-rotation increases, i.e., when the Coriolis effect increases. The relevance of uni-dimensional Ginzburg-Landau models to describe the dynamics of the waves is studied. The domain of validity of these models turns out to be quite narrow.

1 Introduction

Annular shear flows (Fig. 1) represent a class of hydrodynamical systems that permit well-controlled experiments; in particular the fact that no end sections exist simplifies the manipulations. Moreover a Couette flow is obtained in the middle of the channel at low Reynolds numbers. These simplistic hydrodynamic conditions allow the study of more complicated phenomena like interfacial instabilities, when a light fluid is superimposed on top of a heavy fluid [1], or the motion of grains [2,3]. A similar setup with a free surface has been used, in laminar conditions but at higher Reynolds numbers, up to 800, to determine surface shear viscosity, by [4]. Other workers focusing on grain motions [5] or on the hydrodynamics of cohesive sediments [6,7] have run similar setups at Reynolds numbers larger than 10^4, where the flows are turbulent. However, surprisingly, the question of the transition to turbulence in these systems, in the case of a single, Newtonian fluid, has been seldom studied. In [1], Barthelet et al. investigated the flows of a single fluid up to a Reynolds number of 10^3, and concluded that no instability of the axisymmetric flow occurs in that range. One important aim of the present work is to fill the gap between these studies,

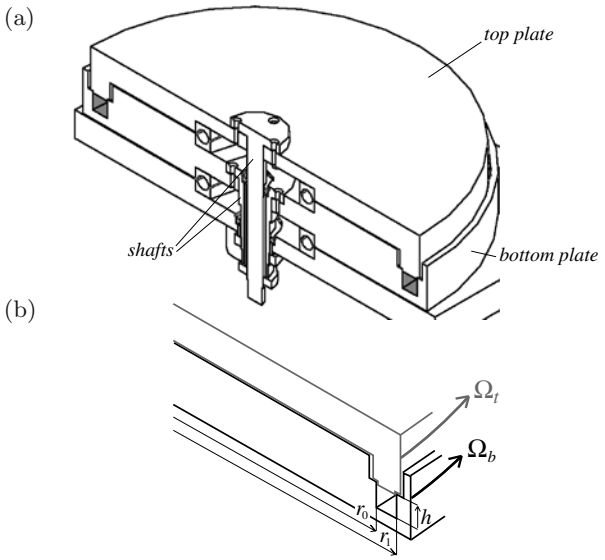

Fig. 1. (a) Global view of the dissected experimental setup: two coaxial PMMA plates rotating independently form an annular channel filled with water (shaded region). Annular shear flows are obtained if only the top plate rotates; rotating annular shear flows are obtained if both plates rotate. (b) Zoom showing the main geometrical and kinematic parameters. Top plate contours and velocity are in gray.

[a] e-mail: emmanuel.plaut@ensem.inpl-nancy.fr

by focusing on the first stage of the transition to turbulence in annular shear flows of a single, Newtonian fluid. Experimental, as well as theoretical results, will be presented.

In order to dispose of a richer system, we will also study the structure and the first instabilities of *rotating* annular shear flows where the plate supporting the channel rotates independently of the lid (Fig. 1). By this way one can introduce inertial forces in the system: the corresponding cases with co-rotation of the two plates, where rotation and shear are present, have therefore some geophysical relevance. Indeed we will see that, when the co-rotation is rapid, an 'Ekman-Couette flow' is obtained at low shear, in the middle of the channel, with the terminology of [8]. One can also study the case of a counter-rotation of the two plates, and we will see that this configuration leads to interesting, new phenomena.

The system used has a small curvature parameter: the ratio Γ of the inter-radii to the mean radius is 9.5% vs. 20% in [1]. This choice has been made to permit, in principle, the use of weakly nonlinear uni-dimensionnal Ginzburg-Landau (GL) models as long as the first transition is to traveling waves. In these models the curvilinear abscissa, the product of the mean radius by the azimuthal angle (see Eq. (14) below), is the only active spatial variable. Such models, given, in the linear regime, by envelope equations of the type (16) below, could be affected, in the nonlinear regime, by the annular topology of the system, see e.g. [9]. One of the motivations of these studies is therefore a test of the validity of these GL models, at first in the linear regime.

The transition to turbulence in similar systems, but where a shear also exists between the two lateral walls (one being fixed, the other being rotated), and the curvature parameter is larger, $\Gamma \gtrsim 60\%$, has been studied by [10]. One speaks then of "annular rotor-stator cavities". We will see that the different geometry, and confinement effects due to the small value of Γ, play an important role at the level of the first instabilities of our annular flows, since these instabilities turn out to be quite different from the ones observed in [10].

In Section 2 we describe the setup and our methods. In Section 3 the basic axisymmetric flows obtained at low shear are characterized, and compared with simple models. For pure shear the corresponding study completes the one of [1], and when the bottom plate rotates this study is novel. The first instabilities of the basic flows, which develop when the shear is increased, are studied in Sections 4 and 5, Section 4 being devoted to the experimental, and Section 5 to the numerical results. The comparison between these two approaches is discussed in the concluding Section 6.

2 System description – Methods

2.1 System description and experimental methods

An experiment has been set up in LEMTA (Fig. 1). In a plate rotating around a vertical axis at the angular velocity Ω_b, a circular channel is dug: its lateral walls are situated at a distance $r_0 = 180$ mm and $r_1 = 198$ mm from the axis. From now on we use cylindrical coordinates (r, φ, z) with r the distance to the rotation axis, φ the azimuthal angle and z the axial coordinate. Above the flat, horizontal bottom ($z = 0$) of the channel, an upper plate rotating around the same axis at the angular velocity Ω_t shears the fluid. The lid, which is the lowest part of this plate, situated in the plane $z = h = 18$ mm, consists of an annulus centered around the mean radius $\overline{r} = 189$ mm, of a width of 17.5 mm. Hence gaps of 250 μm exists between the two sidewalls and the lid. Since the channel contains a newtonian fluid of kinematic viscosity ν, the control parameters are the bottom and top Reynolds numbers

$$Re_b = V_b h/\nu, \qquad Re_t = V_t h/\nu \tag{1}$$

with $(V_b, V_t) = (\Omega_b \overline{r}, \Omega_t \overline{r})$ the plate velocities at mid-radius. Two alternate control parameters are the mean and differential Reynolds numbers

$$\overline{Re} = (Re_b + Re_t)/2, \qquad \delta Re = Re_t - Re_b. \tag{2}$$

The first one $\overline{Re}$ is a dimensionless measure of the co-rotation speed $\overline{\Omega} = (\Omega_b + \Omega_t)/2$. In the cases of fast co-rotation $\overline{Re} \gg 1$ it will be convenient to use a corresponding Ekman number

$$E = \nu/\left(\overline{\Omega} h^2\right) = (\overline{r}/h)/\overline{Re} = 10.5/\overline{Re}. \tag{3}$$

The second parameter δRe is a dimensionless measure of the shear applied to the fluid by the lid.

In practice the two plates are driven by DC motors with reduction units (Motor Diffusion Partner), controlled by servo control cards (Maxon Motor Control). Encoders that generate 50 000 pulses per revolution are used to obtain an accurate measure and control of the rotation speeds. The temperature of the fluid is not regulated but real-time measurements are performed with a thermocouple. In a first stage of this work, we used global visualizations obtained with a CCD video camera placed above the setup. Such images, like the one of Figure 9a, correspond to a domain $r \in [r_0, r_1]$, $\varphi \in [0, 2\pi]$. They require for lighting the use of an annular Neon tube surrounding the bottom plate. This Neon is not completely axisymmetric, and consequently the lighting is not quite homogeneous. Moreover, if the Neon is switched on during more than 1 min, it introduces some slight thermal gradients. To avoid such lighting and thermal gradients, local visualizations, like the one of Figure 9b, obtained still from above but with a cold light source, are interesting. They correspond to $r \in [r_0, r_1]$, $\varphi = \varphi_m$ the measurement angle, which is fixed in the frame of the laboratory. Because of the precise monitoring of the rotation speeds and the temperature, it can be said that the Reynolds numbers (1) are well known and vary of less than 1% during an experiment (at most a few hours). To help the visualizations a tracer, Euperlan PK3000 (Cognis), composed of anisotropic platelike particles, is added in small concentrations of the order of 2×10^{-4} wt. in distilled

water, which is the working fluid. This tracer simultaneously permits laser Doppler velocimetry (LDV) with a Dantec FlowLite system. The beams arrive normally to the outer wall of the bottom plate and are set to measure azimuthal velocities. The measuring volume is 650 μm in length (along the radial direction) and 75 μm in diameter. The Laser is mounted on translation plates that allow a precise positioning of the measuring volume inside the channel. Thus the uncertainties on the position of this volume are $\delta r \simeq 300$ μm, $\delta z \simeq 200$ μm. The system is operated in back-scattering mode.

Since the viscosity of water at 20 °C is $\nu = 1.00\,\mathrm{mm}^2/\mathrm{s}$, a nominal value of the azimuthal velocities for a Reynolds number 1000 is

$$V = Re\,\nu/h \;=\; 55\ \mathrm{mm/s}, \tag{4}$$

which corresponds to an angular frequency $\Omega = V/\overline{r} = 0.29\ \mathrm{rad/s} = 2.8\ \mathrm{rpm}$.

2.2 Numerical modelling

Direct numerical simulations of the incompressible Navier-Stokes equations have been performed with a code based on the pseudospectral Chebyshev-Fourier method presented in [11]. A dimensionless version of the equations is solved in an annulus which has the geometrical characteristics of the experiments, i.e. a square cross-section with $r_1 - r_0 = h$ and $\overline{r} = 10.5h$. In the axial and radial directions Chebyshev polynomials are used on the Gauss-Lobatto grid points, and Fourier expansion is applied in the azimuthal direction. Spatial derivatives are conducted in the spectral space through multiplication by suitable matrices, whereas the advection terms are evaluated at the collocation points through fast transform between spectral and real spaces. This pseudospectral discretization ensures exponential convergence of the solution. The time scheme is semi-implicit and second-order accurate. It is a combination of an explicit treatment (second-order Adams-Bashforth) of the nonlinear terms, and an implicit (backward Euler) discretization for the viscous diffusive terms. The incompressibility condition is imposed through an efficient projection algorithm. A time step involves successive resolution of three Helmholtz equations for the pressure predictor, the velocity and the pressure corrector respectively. A direct solver for these equations is used, based on a complete matrix diagonalization technique. The velocity field obeys no-slip conditions at the boundaries. In the model there are no gaps between the sidewalls $r = r_0,\ r_1,\ z \in\ ]0, h[$ and the lid $r \in\ ]r_0,\ r_1[, z = h$. Therefore, in order to regularize the corresponding velocity jumps, a continuous profile of angular velocity

$$v(r,z)/r = \Omega_b + (\Omega_t - \Omega_b)\exp\left[(z/h-1)/\mu\right] \tag{5}$$

is imposed on the sidewalls. The thickness of regularization $\mu = 0.03$ has been used, but it has been checked that using a lower value of μ does not significantly change for instance global properties of the waves obtained in the case of a pure shear (we shall come back to this in Sect. 5.3). This regularization has already been used and validated in [12].

The grid mesh varies from 64 to 91 and from 49 to 64 points in the radial and axial directions, respectively. In the homogeneous azimuthal direction, the number of Fourier modes varies from 96 to 150, 96 modes meaning that all modes with an azimuthal wavenumber m in the range $[-48, 47]$ are included.

3 Basic axisymmetric flows

Basic axisymmetric flows with a velocity field of the form

$$\boldsymbol{v} = \boldsymbol{V} = U(r,z)\boldsymbol{e}_r + V(r,z)\boldsymbol{e}_\varphi + W(r,z)\boldsymbol{e}_z \tag{6}$$

are obtained when the differential Reynolds number δRe is not too large. Hereafter we analyze the structure of these flows. For this purpose LDV measurements are compared with the numerically computed flows. We also compare our results, whenever possible, with simpler models in unconfined geometries.

3.1 Pure shear: $\mathrm{Re_b} = 0, \mathrm{Re_t} > 0$

At low Reynolds number, for $Re_t \lesssim 100$, a flow that is essentially unidirectionnal, $\boldsymbol{V} = V(r,z)\boldsymbol{e}_\varphi$, is obtained, with a linear profile $V(\overline{r}, z) = V_t z/h$ at mid-radius. This has been shown in Figures 5a, 5b of [1]. This flow is quite similar to the confined Couette flow studied in [13]. When the Reynolds number Re_t becomes larger, nonlinear effects caused by the term $\rho V^2/r$ in the radial component of the Navier-Stokes equation come into play. They drive a centrifugal flow below the lid and a roll in the channel, see Figure 4b of [1] or our Figure 2a. This roll distorts the azimuthal velocity, and consequently a non-monotonous profile $V(\overline{r}, z)$ is obtained at mid-radius. This effect can be seen in Figure 5d of [1]. Our Figure 2 is complementary since it has been obtained at a higher $Re_t = 750$. A computation in similar conditions, which reveals similar effects, has been presented in Figure 3d of [4]; in this last case, the bottom of the channel is rotating instead of the top. A semi-quantitative agreement is obtained between our numerical results and experimental measurements, as shows Figure 2. In Figure 2d and in all subsequent figures showing LDV measurements, the uncertainties on the velocities correspond to the root-mean square of the velocity time-series; for a typical time-series in a basic state, see Figure 7.

The flow displayed in Figure 2d differs significantly from the Batchelor flow that would be obtained between two infinite disks, which has been computed by solving equations (2.5−2.7) of [14] with a shooting method. At higher Reynolds number $Re_t = 1260$, which will turn out to be just below the onset of the first instability (see Sect. 5.3), the numerics show a flow that resembles more the Batchelor flow at least for its azimuthal component (Fig. 3b). However Figure 3a shows radial velocities that

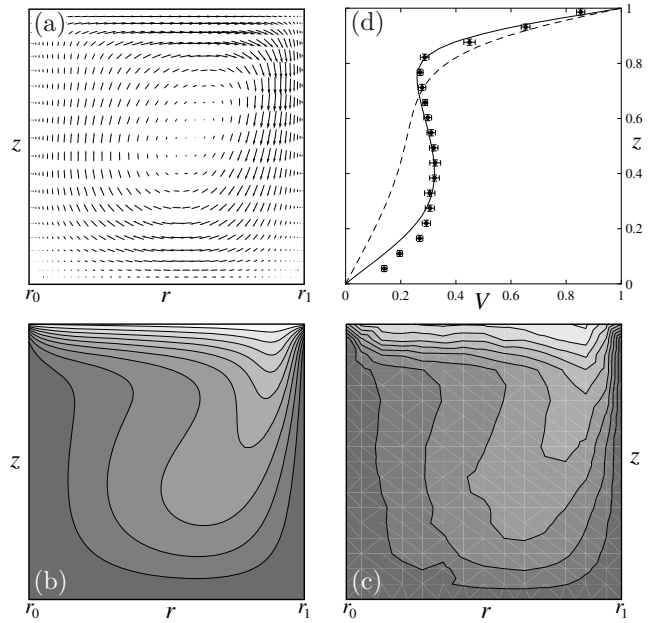

Fig. 2. Basic flow in the pure shear case $Re_t = 750$. (a) Numerical transverse flow; the maximum value of U is $0.078V_t$. (b) Numerical and (c) experimental azimuthal flows; contours at $(0.1, 0.2, \ldots, 0.9)\Omega_t r_1$. (d) Numerical and experimental azimuthal flows at mid-radius $r = \overline{r}$. The unit of V is V_t and the unit of z is h. The dashed line shows the Batchelor flow that would be obtained between two infinite disks.

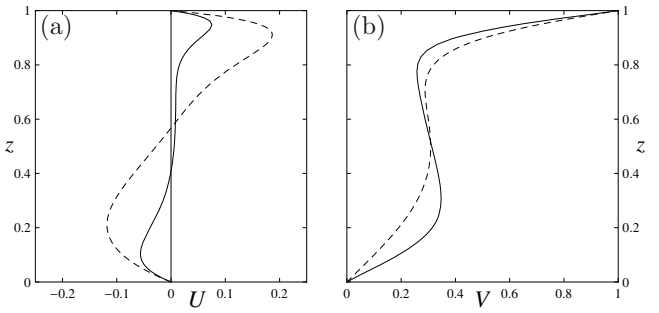

Fig. 3. Basic flow profiles computed in the pure shear case $Re_t = 1260$ and at mid-radius $r = \overline{r}$: (a) radial (b) azimuthal velocity. The unit of velocity is V_t and the unit of z is h. The dashed lines show the Batchelor flow.

are smaller in our confined annulus than between disks; this is clearly an effect due to the influence of the sidewalls. Only at this "high" $Re_t = 1260$ boundary layers (a modified Bödewadt layer above the stationary bottom, a modified Ekman layer below the rotating lid) begin to exist in the middle of the channel ($r = \overline{r}$), but they are not clearly separated.

3.2 Counter-rotation: $\mathbf{Re_t = -Re_b > 0}$

In this case centrifugal effects exist both at the level of the lid and at the level of the bottom. Since the sidewalls

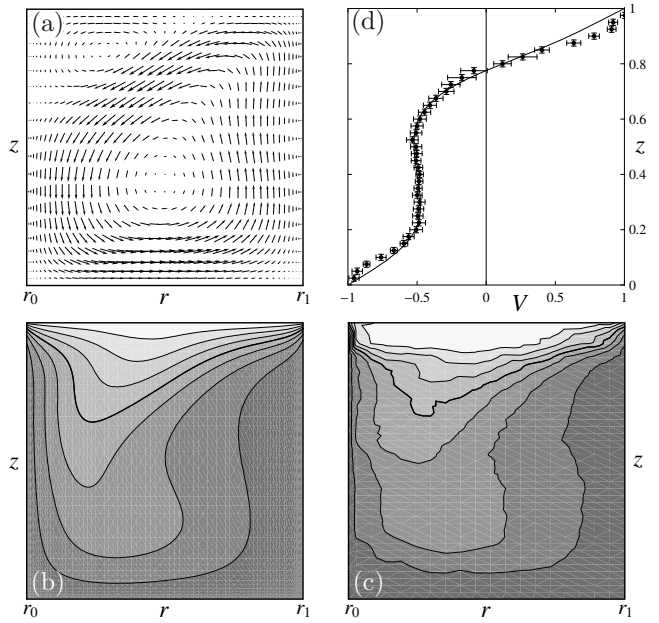

Fig. 4. Basic flow in the counter-rotation case $\delta Re = 1000$. (a) Numerical transverse flow; the maximum value of U is $0.088V_t$. (b) Numerical and (c) experimental azimuthal flows; contours at $(-0.75, -0.5, \ldots, 0.75)\Omega_t r_1$; the thick line is the contour $V = 0$. (d) Numerical and experimental azimuthal flows at mid-radius $r = \overline{r}$. The unit of V is V_t and the unit of z is h.

rotate with the bottom, the roll associated with the bottom is stronger than the one associated with the lid. The ensuing flow, displayed in Figure 4a, distorts the azimuthal velocity field in the manner visible in Figures 4b, 4c. This yields at mid-radius the profile displayed in Figure 4d, the average value of which is negative. In this case also, there is a rather good agreement between the experiments and the numerics.

3.3 Co-rotation: $\mathbf{\overline{Re} > \delta Re > 0}$

A rapid co-rotation of the two plates of the setup introduces strong inertial forces. In agreement with the Proudman-Taylor theorem, one then observes a tendency to form an inviscid core in solid-body rotation. This effect is already visible in Figures 5 and 6a, which correspond to an Ekman number (Eq. (3)) $E = 2.56 \times 10^{-3}$. Figure 6b, for which $E = 5.25 \times 10^{-3}$, 2.56×10^{-3}, 1.75×10^{-3} and 1.31×10^{-3} (from top to bottom), is also demonstrative. In fact we almost recover, in the middle of the channel, at $r = \overline{r}$, an Ekman-Couette flow with the terminology of [8]. This flow can be calculated analytically by disregarding the effects of curvature and of the sidewalls. Considering therefore the flow of a viscous fluid enclosed by two parallel plates (at $z = 0$ and h) co-rotating at $\overline{\Omega} = \frac{1}{2}(\Omega_b + \Omega_t)$, with a velocity difference $\delta V = V_t - V_b$ in the "azimuthal" direction, one can solve the Navier-Stokes equation for this model,

$$2\overline{\boldsymbol{\Omega}} \times \boldsymbol{V} \;=\; \nu \Delta \boldsymbol{V} \;=\; \nu \frac{d^2 \boldsymbol{V}}{dz^2},$$

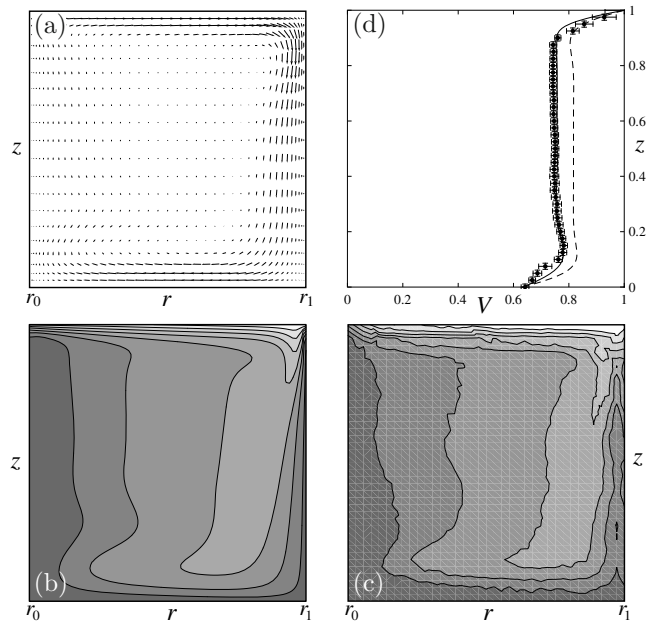

Fig. 5. Basic flow in the co-rotation case $\overline{Re} = 4106$, $\delta Re = 1843$. (a) Numerical transverse flow; the maximum value of U is $0.061V_t$. (b) Numerical and (c) experimental azimuthal flows; contours at $(0.65, 0.70, \ldots, 0.95)\Omega_t r_1$. (d) Numerical and experimental azimuthal flows at mid-radius $r = \overline{r}$. The unit of V is V_t and the unit of z is h. The dashed line shows the Ekman-Couette flow (8).

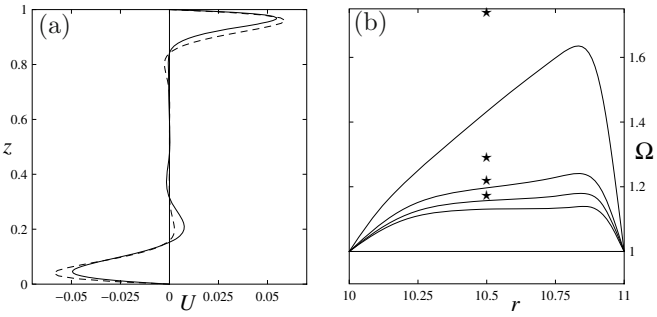

Fig. 6. (a) Radial velocity at mid-radius $r = \overline{r}$ computed in the co-rotation case of Figure 5. The unit of U is V_t and the unit of z is h. The dashed line shows the Ekman-Couette flow (7). (b) Local rotation rates $\Omega = V/r$ at mid-heigth $z = \overline{z} = h/2$ computed for different co-rotation cases, from top to bottom: $(\overline{Re}, \delta Re) = (2000, 1700)$; $(4106, 1843)$; $(6000, 2150)$; $(8000, 2350)$. The stars at mid-radius show the rotation rates $\overline{\Omega}$ that would be obtained in the Ekman-Couette flow (8). The unit of Ω is Ω_b and the unit of r is h.

by using $\boldsymbol{V} = U(z)\boldsymbol{e}_r + V(z)\boldsymbol{e}_\varphi$. This yields

$$\frac{U}{U_0} = \sinh\zeta\sin(\eta-\zeta) - \sin\zeta\sinh(\eta-\zeta), \qquad (7)$$

$$\frac{V-\overline{\Omega}\overline{r}}{U_0} = \cosh\zeta\cos(\eta-\zeta) - \cos\zeta\cosh(\eta-\zeta), \qquad (8)$$

with $2U_0 = \delta V/(\cosh\eta - \cos\eta)$, $\zeta = \eta z/h$ and $\eta = E^{-1/2}$. The fact that the bulk value of the azimuthal velocity in our case is smaller than the one in the Ekman-Couette flow, $\overline{\Omega}\overline{r}$, which is visible in Figures 5d and 6b, is due to the friction at the sidewalls, that rotate with the angular velocity $\Omega_b < \overline{\Omega}$. Figure 6a shows that (7) does describe the radial velocity field at mid-radius rather accurately at $E = 2.56 \times 10^{-3}$. This means that the roll flow displayed in Figure 5a must be seen as a consequence of Coriolis forces more than centrifugal forces.

4 First instabilities: experimental results

When the shear exerted by the lid on the fluid exceeds a critical value, the basic flows (6) may lose their stability. In most cases, these instabilities lead to traveling waves of azimuthal wavenumber m and angular frequency ω. These instabilities can be detected using LDV measurements, though this method does not allow a characterization of the spatial form of the instability. This characterization is done through global (Fig. 9a) and local (Fig. 9b) visualizations, as explained in Section 2.1.

The experimental results are now discussed following the order of presentation of Section 3.

4.1 Pure shear: $\mathrm{Re_b} = 0, \mathrm{Re_t} > 0$

Except in some rare cases, in the early ages of the experiment, forced waves are typically obtained if $Re_b = 0$, $Re_t \gtrsim 1250$, with an angular frequency $\omega \simeq 2\Omega_t$. This forcing at twice the frequency of the rotating plate is quite probably due to a mechanical imperfection of the setup. Typical LDV time series are shown in Figure 7. A wave onset can be defined by plotting

$$A_{\mathrm{LDV}} = \frac{\mathrm{rms}\left[v\left(r_m, \varphi_m, z_m, t\right)\right]}{\left\langle v\left(r_m, \varphi_m, z_m, t\right)\right\rangle_t} \qquad (9)$$

vs. Re_t. In this equation (r_m, φ_m, z_m) designate the coordinates of the measurement "point" (see Sect. 2.1), which is fixed in the frame of the laboratory. The corresponding Figure 8 shows a sharp increase of A_{LDV} above $Re_t \simeq 1250$. In other experiments where the Neon tube is "permanently" switched on, therefore at a higher temperature (of the order of 29 °C vs. 24 °C for the case of Fig. 7) and with some thermal gradients, the apparent threshold measured by LDV is smaller, $Re_t \simeq 1150$. This shows that the slow convection roll that develops in this later case has a destabilizing influence.

Typical visualizations of the waves are shown in Figure 9. The global visualization of Figure 9a proves that the wavenumber $m = 19$. With the terminology of [15,16], this pattern correspond to a "negative" spiral, the angle ε between the azimuthal direction and the spiral arms being of the order of $-4°$. This angle is measured on global visualizations with the unfolded annular geometry. A local visualization at the same Reynolds number using a cold light source yields the spatio-temporal diagram of Figure 9b. The analogy between Figures 9a and 9b is a proof of the

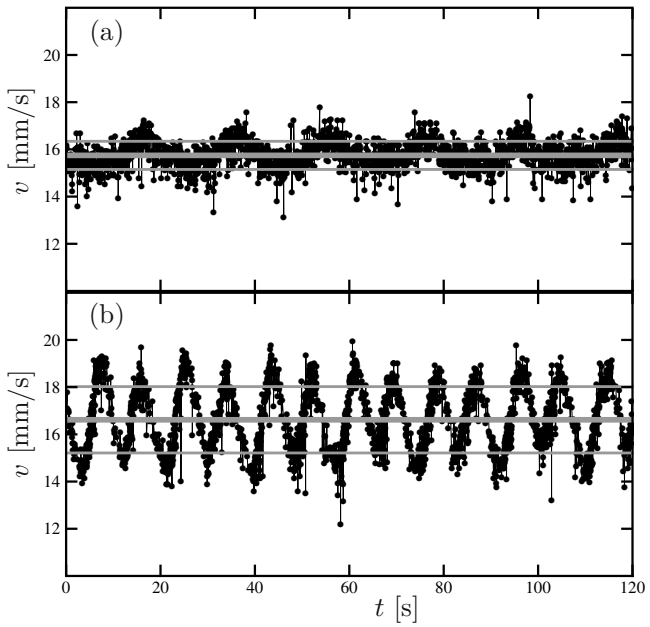

Fig. 7. LDV time series of the azimuthal velocity v obtained at $r_m = 187$ mm $= r_0 + 0.39h$, $z_m = 9$ mm $= 0.5h$ in the pure shear cases (a) $Re_t = 1175$, (b) $Re_t = 1300$. The rotation time of the lid is $T = 20.0$ s in (a), 18.3 s in (b). The noisy oscillation at period T in (a) contrasts with the clear oscillation at half period in (b), which corresponds to a traveling wave. The gray lines show $\langle v \rangle_t$, $\langle v \rangle_t \pm \mathrm{rms}\,(v)$.

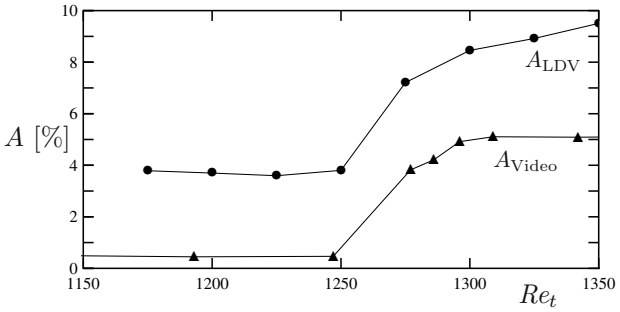

Fig. 8. Wave amplitudes (9) and (10) vs. the top plate Reynolds number in the pure shear case. The points used for the measurements are the one of Figure 7 for A_{LDV}, $r_m = 185.4$ mm $= r_0 + 0.30h$ for A_{Video}.

propagative character of the waves, the fields of which depending only on $X = m\varphi - \omega t$. Therefore a negative $d\varphi$ and a positive dt linked through $m d\varphi = -\omega dt$ lead to the same local intensity. The advantages of the local visualizations like the one of Figure 9b are that a long-lasting illumination can be obtained without introducing thermal gradients (i.e. convection effects), and that the lighting of the (small) region of interest is rather homogeneous. This leads to spatio-temporal diagrams of a better quality. One can extract from these video data, $I \in [0, 1]$ being the intensity measured by the CCD camera, a wave amplitude

$$A_{\mathrm{Video}} = \mathrm{rms}\left[I\left(r_m, \varphi_m, t\right)\right], \qquad (10)$$

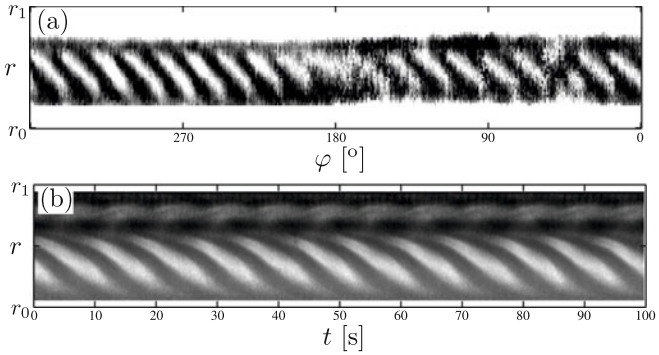

Fig. 9. In the pure shear case $Re_t = 1309$. (a) Global visualization; blurred regions exist since the Neon does not surround the whole channel. (b) Local visualization: spatio-temporal diagram at $\varphi = \varphi_m$. An image of reference in the absence of shear has been substracted.

where the coordinates (r_m, φ_m) of the measurement "point" (the video signal is somehow a z-average) are fixed in the frame of the laboratory. The results visible in Figure 8, that the amplitudes A_{LDV} and A_{Video} both increase sharply around $Re_t = 1250$, confirm that this corresponds to the wave onset. They also validate the use of the Euperlan tracer and local videos to study the first bifurcation, which is apparently supercritical. Waves with a frequency $\omega \simeq 2\Omega_t$ are observed on a large range of Reynolds numbers, $1250 \leq Re_t \lesssim 3500$. A progressive transition to spatio-temporal chaos is obtained at larger Reynolds numbers.

4.2 Counter-rotation: $\mathbf{Re_t = -Re_b > 0}$

When the plates are counter-rotating, and $\delta Re < 980$, the spatio-temporal diagrams obtained with local visualizations show only three horizontal bands associated with the structure of the basic flow. At $\delta Re = 980$, these bands are perturbed by some localized structures, which are excited in an intermittent manner (Fig. 10a). When the shear is increased, these localized structures appear more sharply and more often (Figs. 10b, 10c). A (φ, t) spatio-temporal diagram obtained with global visualizations shows that these structures propagate retrogradely, i.e. in the direction of rotation of the bottom plate, with a phase speed that is not uniform. Thus in this case the first experimental transition is towards spatio-temporal chaos or weak turbulence.

4.3 Co-rotation: $\mathbf{\overline{Re} > \delta Re > 0}$

When the plates are co-rotating, bands associated with the basic flow are also observed at intermediate δRe. An example is visible in Figure 11a, at $\overline{Re} = 1990$, $\delta Re = 1690$, where small modulations are however seen on the band situated around $r = r_0 + 0.4h$. These modulations transform into clear oscillations at $\delta Re = 1790$ (Fig. 11b). Using a Fourier transform of a signal $I(r_m, \varphi_m, t)$, one

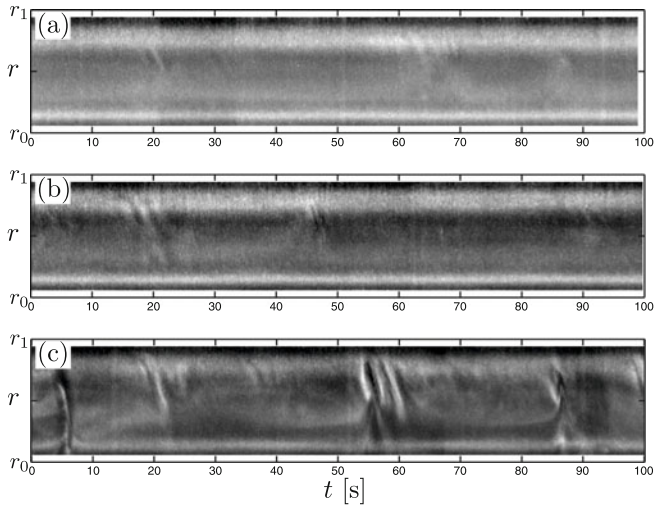

Fig. 10. Local visualizations in the counter-rotation case. (a) At onset of the first instability, $\delta Re = 980$. (b) $\delta Re = 1000$. (c) $\delta Re = 1110$.

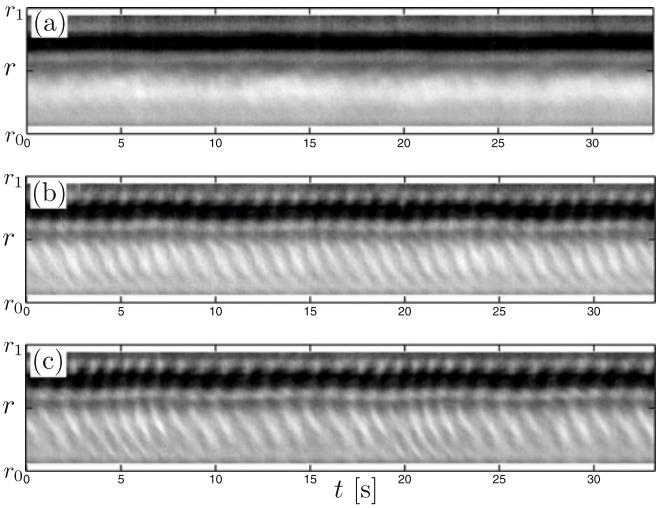

Fig. 11. Local visualizations in the co-rotation case $\overline{Re} = 1990$. (a) At onset of the first instability, $\delta Re = 1690$. (b) $\delta Re = 1790$. (c) $\delta Re = 1890$.

can measure the angular frequency of these oscillations $\omega = 6.3$ rad/s $= 8.3\Omega_t$. At higher $\delta Re = 1890$, the oscillations, of basic frequency $\omega = 5.3$ rad/s $= 6.8\Omega_t$, are modulated (Fig. 11c). Using global visualizations, we found in a similar case $\overline{Re} = 2000$, $\delta Re = 1720$, that the oscillations correspond to prograde traveling waves of wavenumber $m \simeq 20$.

From a geometrical point of view, the waves displayed in Figure 11b are spiralling in opposite directions in the interior ($r < \overline{r}$) and exterior ($r > \overline{r}$) regions of the channel; in the interior one would speak of "negative" spirals, whereas in the exterior one would speak of "positive" spirals. There is a continuity between the spatio-temporal patterns obtained at pure shear (Fig. 9b) and at fast co-rotation (Fig. 11b), as proven by Figure 12. The critical

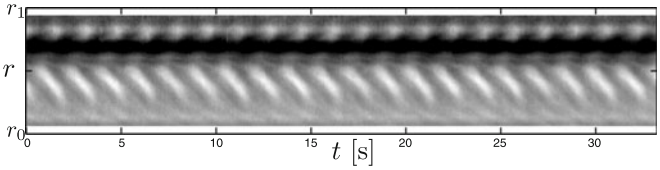

Fig. 12. Local visualization in the co-rotation case $\overline{Re} = 1490$, $\delta Re = 1690$.

parameters of all the cases studied experimentally are displayed in Figure 20, which will be discussed in the concluding section, after the presentation of the theoretical study of the instabilities.

5 First instabilities: numerical results

5.1 Linear modal analyses – Ginzburg-Landau model

From a theoretical point of view, the axisymmetry of the setup and of the basic flows (6) implies that the most dangerous normal modes of perturbation of these basic flows are traveling waves of velocity field

$$\boldsymbol{v} = \mathrm{Re}\left\{A(m,t)\,\boldsymbol{V}_1(r,z)\exp\left[i(m\varphi - \omega_l(m,R)t)\right]\right\} \quad (11)$$

with

$$\boldsymbol{V}_1(r,z) = U_1(r,z)\boldsymbol{e}_r + V_1(r,z)\boldsymbol{e}_\varphi + W_1(r,z)\boldsymbol{e}_z, \quad (12)$$

m the wavenumber, $\omega_l(m,R)$ the angular frequency. Hereafter R designates the shear control parameter, $R = Re_t$ in the pure shear case $Re_b = 0$, $R = \delta Re$ in the other cases, co- or counter-rotation, where $\overline{Re}$ is kept constant. We use a modal analysis method similar to the one of [17] to obtain from direct numerical simulations, starting with the basic flow solution (6) plus small random perturbations, the amplitudes A and the frequencies ω_l. After a short transient, and before trigerring nonlinear effects, only the most dangerous normal modes for each wavenumber m are present in the solution, with amplitudes that assume the form

$$A(m,t) = A_0(m)\exp\left[\sigma_l(m,R)t\right] \quad (13)$$

with $\sigma_l(m,R)$ the growth or decay rate. Thus a post-processing of the spectral numerical results yields, for each case studied, a set of values $\{\sigma_l(m,R), \omega_l(m,R)\}$. By plotting the values of $\sigma_l(m,R)$ a rough estimate of the critical values m_c and R_c at the onset of the instability can be obtained. We then define as close to critical the waves for which m is close to m_c and R is close to R_c. The reduced set of values $\{\sigma_l(m,R), \omega_l(m,R)\}$ thus obtained is then fitted to a uni-dimensional GL model. In this "cartesian" model, the remaining spatial variable is the curvilinear abscissa

$$x = \overline{r}\varphi, \quad (14)$$

and a perturbation velocity component, e.g. the azimuthal velocity, at a given radial and axial position, e.g. in the middle of the channel, is assumed to be given by

$$v\left(\overline{r},\varphi,\overline{z},t\right) = \left[\widetilde{A}(x,t)\exp i\left(k_c x - \omega_c t\right) + c.c.\right] + h.o.t., \quad (15)$$

Table 1. Results of the numerical modal analyses and their fits to the GL model (16). For each case studied the second column recalls the nature of the shear control parameter, and the third column gives the interval of values used for the fits. The prefactors of τ, ω_c and v_g are explained by the choice of viscous time units.

Case	R	$[R_{min}, R_{max}]$	R_c	$(\nu/h^2)\tau$	m_c	ξ/h	E_σ	$(h^2/\nu)\omega_c$	c_0	$(h/\nu)v_g$	c_1	$100E_\omega$
Counter-rot. $\overline{Re} = 0$	δRe	[976, 1000]	980	0.00392	18.2	0.389	3.6%	50.4	−0.224	38.7	0.577	9.9%
Pure shear $Re_b = 0$	Re_t	[1260, 1300]	1270	0.0178	19.9	0.701	4.7%	276	−5.83	315	0.0793	4.6%
Co-rot. $\overline{Re} = 2000$	δRe	[1700, 1750]	1685	0.00733	20.7	0.533	4.1%	2460	8.37	1590	−0.0827	4.6%
Co-rot. $\overline{Re} = 4000$	δRe	[1970, 2080]	1970	0.00462	21.5	0.462	2.5%	6230	6.90	3535	−0.270	3.0%
Co-rot. $\overline{Re} = 6000$	δRe	[2150, 2200]	2185	0.00334	23.3	0.420	1.2%	10 350	5.99	5510	−0.259	0.8%

with $k_c = m_c/\overline{r}$ the cartesian critical wavenumber, ω_c the critical frequency, $\widetilde{A}(x,t)$ the wave envelope. This envelope satisfies the linearized GL equation

$$\tau\left(\partial_t \widetilde{A} + v_g \partial_x \widetilde{A}\right) = (1 + ic_0)\,\epsilon \widetilde{A} + \xi^2 (1 + ic_1)\,\partial_x^2 \widetilde{A} \quad (16)$$

with τ the characteristic time, v_g the group velocity, c_0 the linear frequency shift,

$$\epsilon = R/R_c - 1 \quad (17)$$

the reduced control parameter, ξ the characteristic length, c_1 the dispersion coefficient. A pure wave perturbation of the form (11), (12), (13) corresponds to

$$\widetilde{A} = A_0(m) \exp\left[i\delta k\ x + \sigma_l(m,R)t - i\delta\omega\ t\right] \quad (18)$$

with $\delta k = (m - m_c)/\overline{r}$ the wavenumber, $\delta\omega = \omega_l(m,R) - \omega_c$ the frequency mismatchs. By inserting equation (18) in equation (16), we obtain for the growth or decay rate

$$\sigma_l(m,R) = \sigma_{\mathrm{GL}}(m,R) = \frac{\epsilon}{\tau} - \frac{\xi^2 \delta k^2}{\tau}$$
$$= \frac{1}{\tau}\left(\frac{R}{R_c} - 1\right) - \frac{\xi^2}{\tau \overline{r}^2}(m - m_c)^2 \quad (19)$$

and for the angular frequency

$$\omega_l(m,R) = \omega_{\mathrm{GL}}(m,R) = \omega_c - \frac{c_0\epsilon}{\tau} + v_g\delta k + \frac{\xi^2 c_1 \delta k^2}{\tau}$$
$$= \omega_c - \frac{c_0}{\tau}\left(\frac{R}{R_c} - 1\right) + \frac{v_g}{\overline{r}}(m - m_c)$$
$$+ \frac{\xi^2 c_1}{\tau \overline{r}^2}(m - m_c)^2\,. \quad (20)$$

Polynomial fits of the numerical data $\{\sigma_l(m,R), \omega_l(m,R)\}$ to these laws give the values of R_c, τ, m_c, ξ and ω_c, c_0, v_g, c_1. At least 9 values of $\sigma_l(m,R)$, corresponding to at least 2 different values of R, are used for the fit to (19), and it is checked that the fit is correct to at least 5% in average, i.e. $E_\sigma < 5\%$ with the notations of App. A. The values of $\omega_l(m,R)$ for the same couples (m,R) are then used to fit to (20), and it is found that the fit is correct to at least 0.1% in average, i.e. $E_\omega < 0.1\%$ with the notations of App. A. A summary of the results obtained is given in Table 1. The modal analyses have been performed using viscous time units, which are the most universal units: rotation time units based on the rotation rate Ω_t of the top plate vary with the shear control parameter R. However, once the GL parameters have been determined, it is interesting to rescale the characteristic time and critical frequencies in rotation time units, the group velocity with the top plate velocity, and to form a reduced cartesian phase speed according to

Table 2. Characteristic times, angular frequencies, phase speeds and group velocities deduced from Table 1 by using rotation time units; $T = 2\pi/\Omega_t$ at onset.

Case	τ/T	ω_c/Ω_t	v_φ/V_t	v_g/V_t
Counter-rot. $\overline{Re} = 0$	0.0291	1.08	0.0592	0.0791
Pure shear $Re_b = 0$	0.343	2.28	0.115	0.248
Co-rot. $\overline{Re} = 2000$	0.316	9.08	0.440	0.559
Co-rot. $\overline{Re} = 4000$	0.349	13.1	0.609	0.709
Co-rot. $\overline{Re} = 6000$	0.359	15.3	0.657	0.777

$$\frac{v_\varphi}{V_t} = \frac{1}{m_c}\frac{\omega_c}{\Omega_t}, \quad (21)$$

using in each case the rotation rate corresponding to the critical value of Re_t. This yields the Table 2.

5.2 Pure nonlinear waves

The code has also been run in order to compute pure nonlinear waves with a velocity field of the form

$$\boldsymbol{v} = \boldsymbol{V}_0(r,z) + \mathrm{Re}\left\{\sum_{k=1}^{N} \boldsymbol{V}_k(r,z) \exp\left[ik\left(m\varphi - \omega_n t\right)\right]\right\}. \quad (22)$$

For this purpose all the modes with azimuthal wavenumbers not multiple of m have been cancelled. In (22) both the fields $\boldsymbol{V}_k(r,z)$ and the nonlinear frequency ω_n depend on the basic wavenumber m and on the control parameters. In all cases the numerics show that the bifurcations to the waves is supercritical.

The numerical results are now discussed following the order of presentation of Section 3.

5.3 Pure shear: $\mathbf{Re_b = 0, Re_t > 0}$

The values of $\sigma_l(m, Re_t)$ and $\omega_l(m, Re_t)$ determined with numerical modal analyses are displayed in Figure 13. The

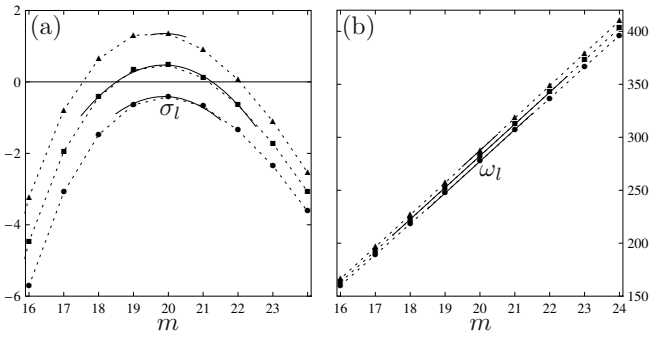

Fig. 13. (a) Growth or decay rates $(h^2/\nu)\sigma_l$ (b) frequencies $(h^2/\nu)\omega_l$ obtained through numerical modal analyses of the pure shear case for $Re_t = 1260$ (disks), 1280 (squares) and 1300 (triangles). The 9 points around which the fits to the GL laws (19) and (20) are shown with continuous lines are the ones that form the data set for these fits.

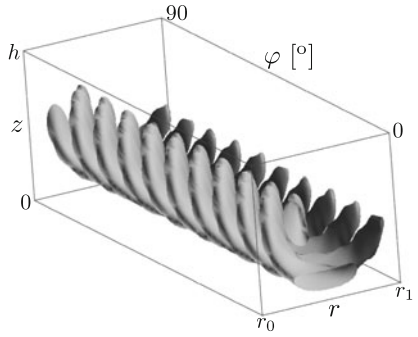

Fig. 14. Surfaces of iso-energy (80% of the maximal energy) of the mode $m = 20$ of a pure nonlinear wave computed for the pure shear case $Re_t = 1296$.

curves $\sigma_l(m, Re_t)$ have a parabolic form only in a narrow range of values of m. Consequently a good fit to (19) (i.e., with $E_\sigma < 5\%$) is obtained if only very few data points are retained. This means that curvature effects are important and preclude the use of the cartesian GL model outside of a very narrow regime. However, the angular frequencies $\omega_l(m, Re_t)$ are rather well described by (20). A three-dimensional view of the local kinetic energy field of a weakly nonlinear wave is shown in Figure 14. This figure shows that the wave fields are larger in the lower half $z < \overline{z}$ of the channel. This explains the rather small value of the phase velocity. The fact that c_0 is large and negative indicates an acceleration of the waves with increasing Re_t, which is not surprising since then the mean flow V in the φ (i.e. x) direction, that advects the waves, becomes larger. The fact that the curves in Figure 13b are almost straight indicates that the waves are almost non dispersive, which is traduced by the small value of c_1.

Another geometrical characterization of the nonlinear wave displayed in Figure 14 can be obtained by plotting slice views of the azimuthal velocity field in planes $z = z_0$. By choosing $z_0 = 0.9h$ we obtain Figure 15. With the terminology of [15,16], this pattern corresponds to a "negative" spiral: the angle ε between the azimuthal direction

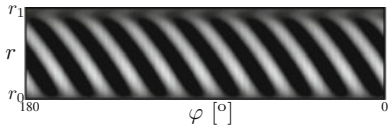

Fig. 15. In the plane $z = 0.9h$, azimuthal velocity field of the wave mode already displayed in Figure 14.

and the spiral arms is of the order of $-10°$. This angle depends on the value of z_0; it typically decreases when z_0 decreases.

Quantitatively, the nonlinear wave of Figures 14 and 15, at $R = Re_t = 1296 = 1.021R_c$, is characterized by

$$|\boldsymbol{V}_1(\overline{r}, \overline{z})| = 0.00560\ V_t \tag{23}$$

and

$$\max_{rz} |\boldsymbol{V}_1(r, z)| = 0.0236\ V_t, \tag{24}$$

this maximum being attained for $r = \overline{r} + 0.03h$, $z = 0.12h$. At a higher $Re_t = 1450$, traveling waves with wavenumbers $m = 18$ and 19 have also been computed. Changing the thickness of regularization μ (Eq. (5)) from 0.03 to 0.02 does not modify the amplitudes and phase velocities of these waves by more than 1.2%. It does not seem interesting to fit these nonlinear results to a nonlinear GL model, since the relevance of the linear GL model is already poor.

5.4 Counter-rotation: $\mathbf{Re_t = -Re_b > 0}$

The numerical modal analyses for this case are shown in Figure 16. As far as the rates σ_l are concerned, the GL model appears to be slightly more relevant than in the pure shear case, since a smaller average error is obtained despite of the use of more data points (compare Figs. 13a and 16a). Figure 17 shows that the waves are now located in the upper part of the channel. When δRe increases, the mean velocities V increase in the upper part of the channel, and this explains why the waves accelerate when δRe increases, i.e., why c_0 is negative. Figure 16b shows that the waves are now strongly dispersive, which is reflected by the fact that c_1 is of order 1. The fact that large variations of the frequencies exist (compare Figs. 13b and 16b) may explain why they are less well described by (20) than in the pure shear case.

The pure nonlinear wave of wavenumber $m = 18$ computed for $R = \delta Re = 1000 = 1.021R_c$ and displayed in Figure 17 is characterized by

$$|\boldsymbol{V}_1(\overline{r}, \overline{z})| = 0.0132\ V_t \tag{25}$$

and

$$\max_{rz} |\boldsymbol{V}_1(r, z)| = 0.0992\ V_t, \tag{26}$$

this maximum being attained for $r = \overline{r} + 0.14h$, $z = 0.85h$. The facts that the characteristic time τ is small (compare the first two lines of Tabs. 1 and 2) and that the wave amplitudes are large (compare Eqs. (23, 24) and (25, 26)) indicate a "violent" instability in this counter-rotation case, as compared with the pure-shear case.

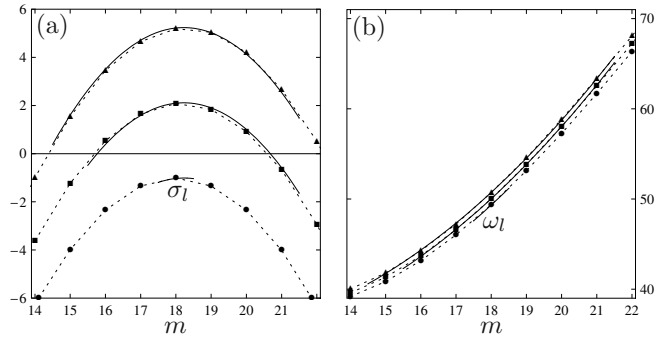

Fig. 16. (a) Rates $(h^2/\nu)\sigma_l$ (b) frequencies $(h^2/\nu)\omega_l$ obtained through numerical modal analyses of the counter-rotation case for $\delta Re = 976$ (disks), 988 (squares) and 1000 (triangles). The continuous lines are the GL fits.

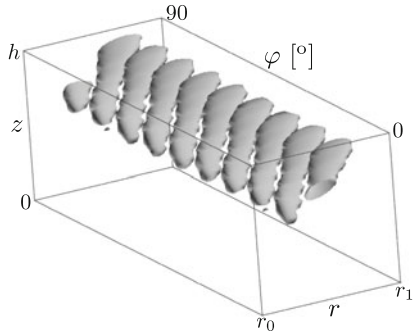

Fig. 17. Surfaces of iso-energy (80% of the maximal energy) of the mode $m = 18$ of a pure nonlinear wave computed in the counter-rotation case $\delta Re = 1000$.

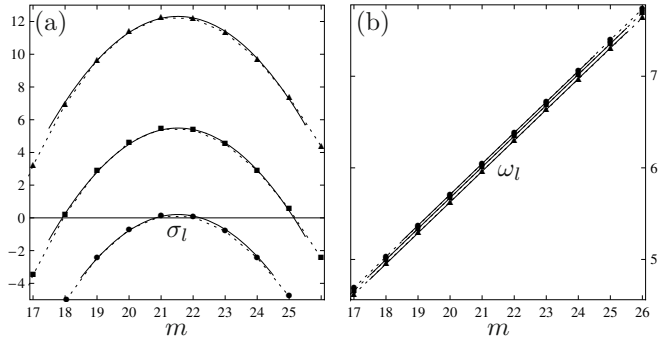

Fig. 18. (a) Rates $(h^2/\nu)\sigma_l$ (b) frequencies $(h^2/\nu)\omega_l/1000$ obtained through numerical modal analyses of the co-rotation case for $\overline{Re} = 4000$, $\delta Re = 1970$ (disks), 2018 (squares) and 2080 (triangles). The continuous lines are the GL fits.

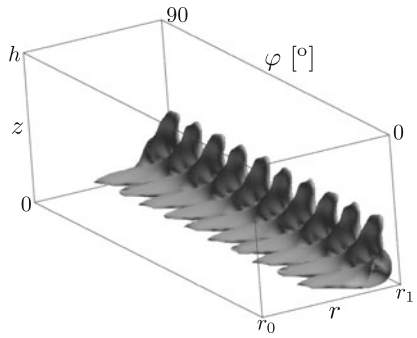

Fig. 19. Surfaces of iso-energy (80% of the maximal energy) of the amplified mode (11) with $m = 21$ computed in the co-rotation case $\overline{Re} = 4000$, $\delta Re = 2000$.

5.5 Co-rotation: $\overline{\mathrm{Re}} > \delta\mathrm{Re} > 0$

The inspection of the last lines of Table 1 proves that, as the co-rotation rate increases, the linear GL model becomes more and more relevant. As an example we show in Figure 18 the numerical modal analyses for $\overline{Re} = 4000$. The rates $\sigma_l(m, \delta Re)$ of the 22 modes considered as close to critical are rather well described by (19), though the values of m and δRe scan a large range as compared with the cases of Figures 13 and 16. Accordingly Figure 18b shows that the frequencies $\omega_l(m, \delta Re)$ of these modes are accurately described by (20). Figure 19 shows that the waves obtained in such co-rotation cases are localized near the lower external part of the channel. Consequently the phase velocity of the waves approaches the azimuthal velocity V_b of the bottom of the channel, as can be seen in Figure 20c. This localization also explains why $c_0 > 0$: when the shear parameter increases (at fixed $\overline{Re}$), V_b and the wave velocity decrease together.

A pure nonlinear wave of wavenumber $m = 21$ computed for $\overline{Re} = 4000$, $R = \delta Re = 2080 = 1.057\ R_c$ is characterized by

$$|\boldsymbol{V}_1(\overline{r}, \overline{z})| = 0.000345\ V_t \tag{27}$$

and

$$\max_{rz} |\boldsymbol{V}_1(r, z)| = 0.0150\ V_t, \tag{28}$$

this maximum being attained for $r = \overline{r} + 0.29h$, $z = 0.067h$. This corresponds to a rather mild instability, as compared with the counter-rotation case of equations (25), (26).

Similarly for $\overline{Re} = 2000$, $\delta Re = 1900 = 1.13\ R_c$, another wave solution of wavenumber $m = 21$ is characterized by

$$|\boldsymbol{V}_1(\overline{r}, \overline{z})| = 0.00137\ V_t \tag{29}$$

and

$$\max_{rz} |\boldsymbol{V}_1(r, z)| = 0.0237\ V_t, \tag{30}$$

this maximum being attained for $r = \overline{r} + 0.23h$, $z = 0.067h$.

For $\overline{Re} = 4000$, an attempt to fit the nonlinear results to a nonlinear GL model,

$$\tau\left(\partial_t \widetilde{A} + v_g \partial_x \widetilde{A}\right) = (1 + ic_0)\,\epsilon \widetilde{A} + \xi^2 (1 + ic_1)\,\partial_x^2 \widetilde{A} - \gamma(1 + ic)\left|\widetilde{A}\right|^2 \widetilde{A}, \tag{31}$$

has been performed, but it turns out that this model is relevant only for a quite narrow wavenumber band, $m \in [20, 21]$. By adding data obtained with $m = 19$ for instance, we observe some errors on the saturated amplitude of the waves (like the ones given in Eqs. (29) and (30)) of

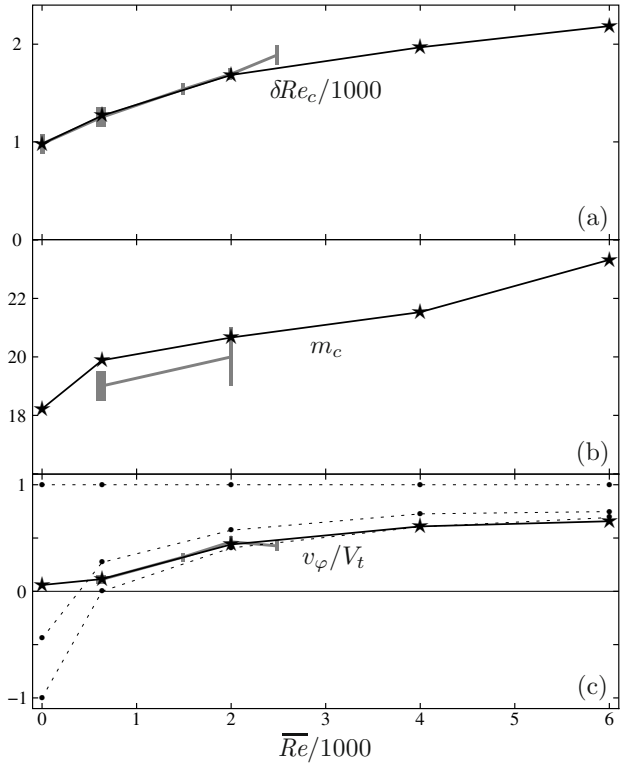

Fig. 20. (a) Critical value of δRe (b) critical wavenumber (c) critical phase velocities at the onset of the first instabilities. The continuous black curves and the stars show the numerical results, the continuous gray curves the experimental results; the dimensions of the boxes correspond to the errorbars. In (c) the dotted curves show the ratii V_b/V_t (lowest curve), $\langle V\rangle_{rz}/V_t$ (mid curve) and V_t/V_t (upper curve) characterizing the basic flows at onset according to the numerics.

the order of 16%. Things are even worse when it comes to the modelling of the nonlinear frequencies ω_n, which are typically only slightly larger than the linear frequencies ω_l.

6 Concluding discussions

Before discussing the general properties of the first instabilities, we precise the relevance of the GL models, since they are used numerically to determine the critical parameters of the first instabilities. We then compare with other systems, and conclude with one open question.

6.1 Relevance of the Ginzburg-Landau models

One conclusion of the numerical study is that the GL model (31) is only valid in quite narrow wavenumber and Reynolds number bands. Therefore, the GL model should be used only in the linear regime (i.e., its linearized version given by Eq. (16) is sufficient), to extract the critical parameters of the first instabilities from the direct numerical simulations.

Indeed, even in the favourable case of fast co-rotation, where at the linear level the wavenumber band of relevance is "large", the agreement between the numerics and the GL model is destroyed at the nonlinear level, even for pure waves, since their frequency and saturated amplitude are poorly described (Sect. 5.5). This means that the question of nonlocal nonlinear effects in GL models, such as the ones evidenced theoretically in [9], is irrelevant for this system. Indeed local and nonlocal GL models coincide for pure waves with the local model (31); if this equation is not relevant for pure waves then both GL models are irrelevant.

The fact that the GL models are poorly relevant is probably explained by the fact that the separation between the small scales of the instability, i.e., $h = r_1 - r_0$, and the large scales of the modulations, i.e., $L_x = 2\pi\overline{r}$, is not large enough. In other words, the curvature parameter $\Gamma = h/\overline{r} = 0.095$ is still too large, i.e. curvature effects are too strong for the GL model to be highly relevant. It would be interesting to test this idea by studying a system with a smaller curvature parameter.

6.2 General properties of the first instabilities

A comparison between the critical parameters of the first instabilities determined experimentally and the ones obtained numerically is performed in Figure 20. The thresholds of the instabilities have been estimated experimentally from the study of the curves $A_{\rm LDV}$ and $A_{\rm Video}$ as explained at the level of Figure 8. As far as δRe_c is concerned, a good agreement between the numerics and the experiments is observed for $\overline{Re} \lesssim 2000$ (Fig. 20a). The value of the critical Reynolds number obtained in the pure shear case, $Re_c = \delta Re_c \simeq 1260$, is consistent with the observation made in a similar system, that the flow is laminar at $Re = 1000$ [1]. The discrepancy between the numerics and the experiments at large $\overline{Re}$, which is visible in Figure 20a, is probably due to the fact that the waves at large $\overline{Re}$ saturate at a very low amplitude (see the remark after Eq. (28)), and are therefore quite difficult to detect experimentally. This is confirmed by the low level of $A_{\rm LDV}$ obtained experimentally for $\overline{Re} = 2000$, $\delta Re = 1900 = 1.12\delta Re_c$, $A_{\rm LDV} \simeq 4\%$ at most (in the region where it is maximal, $r = r_m \simeq 196$ mm, $z = z_m \simeq 6$ mm), to be compared to $A_{\rm LDV} \simeq 9\%$ at $\overline{Re} = 675$, $\delta Re = 1350 \simeq 1.08\delta Re_c$ (Fig. 8).

Measurements of the wavenumber m_c at onset require global visualizations, which are delicate: the lighting is not homogeneous, and, especially at large $\overline{Re}$, the low amplitude waves are difficult to visualize at all angles $\varphi \in [0, 2\pi]$. Therefore we could only perform two measurements of m_c (Fig. 20b). The measured wavenumbers are smaller than the ones predicted numerically, but by less than one unit; there is hence a semi quantitative agreement between the theory and the experiments at this level.

One can extract from the time series obtained with LDV or video the angular frequency ω_c of the oscillations at or slightly above onset. Using the experimentally measured wavenumbers whenever possible, or the theoretical

value m_c in the other cases, one can define an "experimental" value of the phase speed according to the formula (21),

$$\frac{v_\varphi^{\text{expe}}}{V_t} = \frac{1}{m_c^{\text{expe or theo}}} \frac{\omega_c^{\text{expe}}}{\Omega_t}. \quad (32)$$

These phase speeds are compared with theoretical values in Figure 20c. Here also a good agreement is observed between experiments and theory. The fact that the phase velocities of the waves approach V_b at large $\overline{Re}$ is coherent with their localization in the bottom of the channel (Fig. 19).

6.3 Comparisons with other systems

The localization near a corner visible in Figure 19 precludes a comparison with theoretical stability analyses performed in non confined geometries, such as the ones of [8,18]. At lower $\overline{Re}$, the waves are less localized, but still clearly influenced by the sidewalls, see e.g. Figure 14. Hence in this case also results in non confined geometries should be irrelevant. This is confirmed by the fact that, in the pure shear case, the structure of the instability at onset, i.e. slightly negative spirals (Figs. 9 and 15), has nothing to do with the structures observed by [10] in a less confined setup, i.e. circular rolls and positive spirall rolls.

The curvature of our system also plays an important role. Indeed, the study of [13] showed that the confined Couette flow in a straight channel sheared by a lid is linearly stable whatever the Reynolds number, i.e. the transition to turbulence is subcritical in this case. This contrasts with the supercritical Hopf bifurcation obtained in the pure shear case in our system. It can be argued, on the basis of this observation, that the curvature of our system has a destabilizing influence.

6.4 Open question

The rather good agreement obtained between experiments and theory as far as the critical parameters of the first instabilities are concerned, which is visible in Figure 20, should not hide the fact that our understanding of the scenario in the counter-rotation case ($\overline{Re} = 0$) is poor. Indeed the theoretical approach used here assumes that the instabilities are wavy, which is not confirmed by the experiments in this particular case (Fig. 10). It would be interesting to perform nonlinear direct numerical simulations retaining all wavenumbers in this case.

We thank J.-P. Brancher and B. Rémy for fruitful discussions and help. E.P. and Y.L. thank J.-R. Angilella (in connection with the PPF Chaos) for his financial support, J.-Y. Morel and A. Delconte for their technical support. This work was granted access to the HPC resources of IDRIS under the allocation 2007-0242 made by GENCI (Grand Equipement National de Calcul Intensif).

Appendix A: Definition of average errors for the Ginzburg-Landau fits

It is important to quantify the quality of the fits of the data $\{\sigma_l(m,R), \omega_l(m,R)\}$ obtained with a numerical modal analysis to the GL predictions (19) and (20). For this purpose we note $\mathcal{M}(R)$ the set of the values of m for which such data are considered at fixed R, $M(R)$ the cardinality of this set, and define nominal values of $|\sigma_l(m,R)|$ and $\omega_l(m,R)$ as follows:

$$\langle|\sigma(R)|\rangle = \left[\sum_{m\in\mathcal{M}(R)} |\sigma_l(m,R)|\right] /M(R),$$

$$\langle\omega(R)\rangle = \left[\sum_{m\in\mathcal{M}(R)} \omega_l(m,R)\right] /M(R).$$

Denoting with $M_{tot} = \sum_R M(R)$ the total number of data points, we define the average errors E_σ and E_ω by

$$M_{tot}E_\sigma = \sum_R \sum_{m\in\mathcal{M}(R)} \frac{|\sigma_l(m,R) - \sigma_{\text{GL}}(m,R)|}{\langle|\sigma(R)|\rangle},$$

$$M_{tot}E_\omega = \sum_R \sum_{m\in\mathcal{M}(R)} \frac{|\omega_l(m,R) - \omega_{\text{GL}}(m,R)|}{\langle\omega(R)\rangle}.$$

References

1. P. Barthelet, F. Charru, J. Fabre, J. Fluid Mech. **303**, 23 (1995)
2. F. Charru, H. Mouilleron, O. Eiff, J. Fluid Mech. **519**, 55 (2004)
3. F. Charru, E. Larrieu, J.B. Dupont, R. Zenit, J. Fluid Mech. **570**, 431 (2007)
4. A.H. Hirsa, J.M. Lopez, R. Miraghaie, J. Fluid Mech. **470**, 135 (2002)
5. A. Betat, V. Frette, I. Rehberg, Phys. Rev. Lett. **83**, 88 (1999)
6. M.K. Fukuda, W. Lick, J. Geophys. Res. **85**, 2813 (1980)
7. C.L. Amos, J. Grant, G.R. Daborn, K. Black, Estuar. Coast. Shelf Sci. **34**, 557 (1992)
8. N. Hoffmann, F.H. Busse, W.L. Chen, J. Fluid Mech. **366**, 311 (1998)
9. E. Plaut, Phys. Rev. E **67**, 046303 (2003)
10. S. Poncet, E. Serre, P.L. Gal, Phys. Fluids **21**, 064106 (2009)
11. I. Raspo, S. Hugues, E. Serre, A. Randriamampianina, P. Bontoux, Comput. Fluids **31**, 745 (2002)
12. E. Serre, P. Bontoux, B.E. Launder, Flow Turbul. Combust. **69**, 35 (2002)
13. V. Theofilis, P.W. Duck, J. Owen, J. Fluid Mech. **505**, 249 (2004)
14. G.N. Lance, M.H. Rogers, Proc. R. Soc. Lond. A **266**, 109 (1962)
15. L. Schouveiler, P.L. Gal, M.P. Chauve, J. Fluid Mech. **443**, 329 (2001)
16. G. Gauthier, P. Gondret, F. Moisy, M. Rabaud, J. Fluid Mech. **473**, 1 (2002)
17. J.D. Scheel, M.R. Paul, M.C. Cross, P.F. Fischer, Phys. Rev. E **68**, 066216 (2003)
18. A. Faller, J. Fluid Mech. **230**, 245 (1991)